Techset Composition Ltd, Salisbury
Doc: {IEE}RSN/Articles/Pagination/RSN58020.3d

www.ietdl.org

Published in IET Radar, Sonar and Navigation
Received on 10th June 2008
Revised on 16th April 2009
doi: 10.1049/iet-rsn.2008.0086

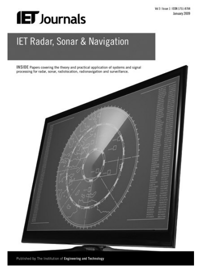

ISSN 1751-8784

Scatterers characterisation in radar imaging using joint time–frequency analysis and polarimetric coherent decompositions

M. Duquenoy[1,2] *J.P. Ovarlez*[1,3] *L. Ferro-Famil*[2] *E. Pottier*[2] *L. Vignaud*[1]

[1]*ONERA, Electromagnetism and Radar Department, Chemin de la Hunière, F-91761 Palaiseau Cedex, France*
[2]*Image and Remote Sensing Group, Institute of Electronics and Telecommunications from Rennes, University of Rennes 1, Campus Beaulieu, Bat 11D, 263 Avenue Général Leclerc, CS-74205 Rennes Cedex, France*
[3]*SONDRA, Supelec, France*
E-mail: jeanphilippe.ovarlez@mac.com

Abstract: Classical radar imaging generally considers targets as set of isotropic independent sources with a constant response in the measured frequency band. Nevertheless, new radar capabilities, in terms of signal bandwidth and angular excursion, may challenge this bright point model. Studies based on multidimensional time–frequency (TF) analysis, describing the angular and frequency behaviour of a scene's reflectivity, showed that some scatterers may have anisotropic and dispersive responses. Polarisation diversity is an interesting additional source of information in radar imaging, and provides indicators closely linked to some geometric and electromagnetic properties of the observed objects. In this study, a fully polarimetric TF analysis is proposed for radar imaging (SAR, ISAR) that characterises the anisotropic and dispersive behaviour of the polarimetric response of deterministic targets. This method is based on the hyper-image concept, which describes the response of scatterers as a function of the observation angle, the emitted frequency and polarimetric canonical behaviours. Polarimetric hyper-images point out that non-stationary behaviours can be related to physical properties of the target (geometrical shape, relative orientation) and allow a better understanding of the scattering mechanisms. This polarimetric hyper-image representation is then used to detect non-stationary scatterers and to classify their behaviour.

1 Introduction

Radar is an instrument traditionally used to pinpoint the position and velocity of a target from its backscattered microwave energy. Synthetic aperture radar (SAR) images represent maps of the spatial distribution of the reflectivity of a scene. High-range resolution may be obtained in the range direction by emitting waveforms with a large bandwidth of the transmitted waveform, whereas high cross-range resolution is achieved by coherently processing returned signals from correlated sequences of small apertures at different aspect angles of the radar in order to synthesise a large aperture [1].

Conventional radar imaging techniques consider targets as a set of bright points. Indeed, scatterers are considered to have an isotropic response, constant over the frequency band described by the signal waveform [2, 3]. Recent studies, based on time–frequency (TF) analysis, demonstrated how to estimate the spatial distribution of the angular and frequency behaviours of a scene imaged by a SAR [4–6]. These representations, called hyper-images, showed that some scatterers were neither isotropic nor white in the frequency domain. Such non-stationary behaviours may be particularly frequent over images acquired by modern high-resolution SAR sensors using large frequency band width and azimuth beam width. The varying response of scatterers may be due to material dispersion or dispersive or anisotropic effects induced by their geometry or their orientation.

Polarimetry is another information source about the geometry and the orientation of scatterers in radar imaging. We are specially interested in its application on man-made targets, because they present a dispersive and anisotropic behaviour. We use polarimetric coherent decompositions [7], which express the scattering or Sinclair matrix as a combination of the scattering responses of simpler objects, as a primary tool to compare the geometry of scatterers to those of canonical objects, and to get notions on their orientation.

The goal is to combine TF analysis and polarimetry in order to obtain a better understanding of the backscattering mechanisms and to explain the non-stationary behaviour of scatterers. In this context, two approaches are possible. The first consists in using TF analysis and polarimetry separately, and to merge their data in a second time. The problem raised by this first approach is that data can be redundant. The second proposes to use TF analysis and polarimetry jointly. This technique consists in decomposing processed polarimetric radar images into frequency/angular/polarisation information of the image scatterers (called polarimetric hyper-image).

In this paper, a fully polarimetric TF analysis method is proposed to describe the polarimetric nature relative to the angle of illumination and the emitted frequency. The polarimetric hyper-images construction is explained from the classical radar imaging, the 2D TF analysis and the coherent decompositions. Then, polarimetric hyper-images are applied to full polarimetric anechoic chamber data. Finally, we extract statistics that characterise the dispersive behaviour, the anisotropic behaviour and the non-stationary polarimetric behaviour, and use them to process a classification.

2 Classical radar imaging

The backscattering coefficient $H(\boldsymbol{k})$ of an object illuminated by a radar is defined as

$$H(\boldsymbol{k}) = \lim_{R\to\infty} \sqrt{4\pi R^2}\frac{E_\mathrm{r}}{E_\mathrm{i}} \tag{1}$$

where E_r and E_i represent the complex amplitude of the incoming and reflected field, respectively, and R stands for the distance between the radar and the object.

The squared modulus of $H(\boldsymbol{k})$ is called the radar cross section (RCS) and is expressed in squared metres. The two-dimensional (2-D) wave vector, $\boldsymbol{k}$, is related to the frequency f and to the direction θ of illumination by $|\boldsymbol{k}| = k = 2\pi f/c$ and $\theta = \arg(\boldsymbol{k})$.

Under the bright point model assumption, commonly used in radar imaging [8], the object under analysis is considered as a set of ideal independent reflectors, that is independent point whose reflection properties remain constant over the measured frequency domain and for all directions of presentation. Let $S(\boldsymbol{r})$ be the complex amplitude of the bright point response located at $\boldsymbol{r} = (x, y)^\mathrm{T}$ in a set of Cartesian axes related to the object. Under far field conditions, the complex backscattering coefficient for the whole object is given by the in-phase summation of each reflector contribution

$$H(\boldsymbol{k}) = \int S(\boldsymbol{r})\,\mathrm{e}^{-2i\boldsymbol{k}.\boldsymbol{r}}\,\mathrm{d}\boldsymbol{r} \tag{2}$$

After a Fourier transform of (2), one can obtain the spatial distribution $S(\boldsymbol{r})$ of the complex amplitude of the scatterers' response around the centre frequency and mean angle of presentation

$$S(\boldsymbol{r}) = \int H(\boldsymbol{k})\,\mathrm{e}^{2i\boldsymbol{k}.\boldsymbol{r}}\,\mathrm{d}\boldsymbol{k} \tag{3}$$

The spatial distribution of the backscattered energy is denoted by

$$I(\boldsymbol{r}) = |S(\boldsymbol{r})|^2 \tag{4}$$

The polarimetric generalisation of the scattering coefficient is called the scattering matrix $\boldsymbol{S}$ or Sinclair matrix, defined in the polarimetric horizontal–vertical basis, as

$$\boldsymbol{S} = \begin{bmatrix} S_{hh} & S_{hv} \\ S_{vh} & S_{vv} \end{bmatrix} \tag{5}$$

where S_{pq} represents the target response in the polarimetric axis p to an incoming wave polarised along the axis q.

One may realistically expect that the response of some scatterers, illuminated over a large frequency domain and/or a large angular extent, may vary with the acquisition parameters. The corresponding coherent (complex amplitude) or incoherent (energy) reflectivity spatial distributions may then depend on the considered wave vector $\boldsymbol{k}$ and will be denoted as $S(\boldsymbol{r}, \boldsymbol{k})$ and $I(\boldsymbol{r}, \boldsymbol{k})$, respectively, in the sequel.

3 Extended radar imaging

Extended radar images can be constructed using TF analysis and physical group theory [5]. The dimension of the resulting hyper-images is the product of the dimension of the spatial vector $\boldsymbol{r}$ by the dimension of the spectral vector $\boldsymbol{k}$.

The principle of extended radar imaging is based on a physical group of transformations, the similarity group $\mathcal{S}$,

IET Radar Sonar Navig., pp. 1–19
doi: 10.1049/iet-rsn.2008.0086

that acts on the physical variables $\boldsymbol{r}$ and $\boldsymbol{k}$ through rotation $[\boldsymbol{R}]_\alpha$, dilatation a and translation $\delta\boldsymbol{r}$ as

$$\begin{array}{ccc} \boldsymbol{r} & \longrightarrow & \boldsymbol{r}' = a\,[\boldsymbol{R}]_\alpha\,\boldsymbol{r} + \delta\boldsymbol{r} \\ \downarrow & & \downarrow \\ \boldsymbol{k} & \longrightarrow & \boldsymbol{k}' = a^{-1}\,[\boldsymbol{R}]_\alpha\,\boldsymbol{k} \end{array} \tag{6}$$

The transformation laws for the reflected signal $H(\boldsymbol{k})$ and its extended image $I(\boldsymbol{r}, \boldsymbol{k})$ are therefore given by

$$\begin{array}{ccc} H(\boldsymbol{k}) & \longrightarrow & H'(\boldsymbol{k}) = a\exp(-2i\boldsymbol{k}\cdot\delta\boldsymbol{r})\,H(a[\boldsymbol{R}]_\alpha^{-1}\,\boldsymbol{k}) \\ \downarrow & & \downarrow \\ I(\boldsymbol{r}, \boldsymbol{k}) & \longrightarrow & I'(\boldsymbol{r}, \boldsymbol{k}) = I(a^{-1}\,[\boldsymbol{R}]_\alpha^{-1}\,(\boldsymbol{r} - \delta\boldsymbol{r}),\, a\,[\boldsymbol{R}]_\alpha^{-1}\,\boldsymbol{k}) \end{array} \tag{7}$$

This covariance law depicts the invariance of the form of physical laws under arbitrary differentiable coordinate transformations.

In radar imaging, the most commonly used changes of reference coordinates are the shift of the reference origin (translation $\delta\boldsymbol{r}$), the modification of the axis orientation (rotation $[\boldsymbol{R}]_\alpha$), and the change of scale (dilatation a in space or time). Two different acquisition configurations, $\mathcal{A}$ and $\mathcal{B}$, characterised by their spatial coordinate system, $\boldsymbol{r}$ and $\boldsymbol{r}'$, respectively, have spectral coordinate systems, $\boldsymbol{k}$ and $\boldsymbol{k}'$, given by the transformation law in (6). The measured backscattering coefficients, $H(\boldsymbol{k})$ and $H'(\boldsymbol{k})$, and the corresponding extended images, $I(\boldsymbol{k})$ and $I'(\boldsymbol{k})$, are related by the covariance law given in (7).

3.1 General formulation of extended images

A first approach to derive the energy distribution $I(\boldsymbol{r}, \boldsymbol{k})$ consists in representing it as a hermitian and bi-linear form of the signal $H(\boldsymbol{k})$ reflected by the target

$$I(\boldsymbol{r}, \boldsymbol{k}) = \int\!\!\int K(\boldsymbol{k}_1, \boldsymbol{k}_2, \boldsymbol{r}, \boldsymbol{k})\,H(\boldsymbol{k}_1)\,H^*(\boldsymbol{k}_2)\,\mathrm{d}\boldsymbol{k}_1\,\mathrm{d}\boldsymbol{k}_2 \tag{8}$$

where the hermitian kernel $K(\boldsymbol{k}_1, \boldsymbol{k}_2, \boldsymbol{r}, \boldsymbol{k})$ can be chosen so as to satisfy physical constraints made on the distribution $I(\boldsymbol{r}, \boldsymbol{k})$:

- the distribution can satisfy the property of covariance by the similarity group $\mathcal{S}$,

- $I(\boldsymbol{r}, \boldsymbol{k})$ can be considered, in $\mathbb{R}^2$, as a spatial density of energy (for a given $\boldsymbol{k}$), implying a constraint of positiveness. Its integration over a spatial region $\mathcal{D}$ can, therefore, be interpreted as the RCS contribution $\sigma_{\mathcal{D}}(\boldsymbol{k})$ of all the reflectors contained in $\mathcal{D}$

$$\sigma_{\mathcal{D}}(\boldsymbol{k}) = \int_{\mathcal{D}} I(\boldsymbol{r}, \boldsymbol{k})\,\mathrm{d}\boldsymbol{r} \tag{9}$$

- if $\mathcal{D}$ represents the whole spatial domain, the distribution can respect the well known marginal property

$$\int I(\boldsymbol{r}, \boldsymbol{k})\,\mathrm{d}\boldsymbol{r} = |H(\boldsymbol{k})|^2 \tag{10}$$

- the conservation of energy between the distribution and the reflected signal spaces leads to an important relation (Moyal formula) that connects the inner product between two given reflected signals H_1 and H_2 and their associated distributions I_1 and I_2

$$\left|\int H_1(\boldsymbol{k})\,H_2^*(\boldsymbol{k})\,\mathrm{d}\boldsymbol{k}\right|^2 = \int\!\!\int I_1(\boldsymbol{r}, \boldsymbol{k})\,I_2^*(\boldsymbol{r}, \boldsymbol{k})\,\mathrm{d}\boldsymbol{r}\,\mathrm{d}\boldsymbol{k} \tag{11}$$

Studies on TF analysis have shown that no distribution can satisfy simultaneously all these properties [9]. As an example, kernels satisfying property (11) do not always lead to positive distributions, and are inconsistent with the RCS nature of the distribution given by (9) or (10).

To overcome this drawback, it is possible to construct a regularised form by smoothing the general distribution given in (8). These regularised distributions verify the covariance property, the RCS property (9) and the Moyal formula (11) but not the marginalisation property (10). The construction of such regularised extended images using a wavelet transform is developed in the next section.

3.2 Construction of extended images by wavelet transform

Let $\phi(\boldsymbol{k}) = \phi(k, \theta)$ be a mother wavelet representing the signal reflected by a reference target. The associated distribution $I_\phi(\boldsymbol{r}, \boldsymbol{k})$ is supposed to be well located around the spatial origin $\boldsymbol{r} = 0$ and the spectral location $(k, \theta) = (1, 0)$. One can, for instance, use a (2-D) separate Gaussian function

$$\phi(k, \theta) = \exp\left(-\frac{(k-1)^2}{\sigma_k^2}\right)\exp\left(-\frac{\theta^2}{\sigma_\theta^2}\right) \tag{12}$$

where the two free parameters σ_k and σ_θ control the spread in frequency and in angular domain and relations between spatial and spectral resolutions.

Using the similarity group, $\mathcal{S}$, a family of wavelet bases $\Psi_{\boldsymbol{r}_0,\boldsymbol{k}_0}(\boldsymbol{k})$ can be generated from the mother wavelet $\phi(k, \theta)$ as

$$\begin{aligned} \Psi_{\boldsymbol{r}_0,\boldsymbol{k}_0}(\boldsymbol{k}) &= \frac{1}{k_0}\exp(-2i\boldsymbol{k}\boldsymbol{r}_0)\,\phi\left(\frac{1}{k_0}\,[\boldsymbol{R}]_{\theta_0}^{-1}\,\boldsymbol{k}\right) \\ &= \frac{1}{k_0}\exp(-2i\boldsymbol{k}\boldsymbol{r}_0)\,\phi\left(\frac{k}{k_0},\, \theta - \theta_0\right) \end{aligned} \tag{13}$$

A regularised distribution $I_\mathrm{r}(\boldsymbol{r}_0, \boldsymbol{k}_0)$ can be built by smoothing the general distribution $I(\boldsymbol{r}, \boldsymbol{k})$ given by (8). Using the Moyal formula (11), the covariance property with $H_1(\boldsymbol{k}) = H(\boldsymbol{k})$, $H_2(\boldsymbol{k}) = \Psi_{\boldsymbol{r}_0,\boldsymbol{k}_0}(\boldsymbol{k})$, $I_1 = I_H$ and $I_2 = I_\phi$, we obtain

$$\begin{aligned} I_{\mathrm{r}}(\boldsymbol{r}_0, \boldsymbol{k}_0) &= \iint I_H(\boldsymbol{r}, \boldsymbol{k})\, I_\phi^*\left(k_0[\boldsymbol{R}]_{\theta_0}^{-1}(\boldsymbol{r}-\boldsymbol{r}_0), \frac{1}{k_0}[\boldsymbol{R}]_{\theta_0}^{-1}\boldsymbol{k}\right)\mathrm{d}\boldsymbol{r}\,\mathrm{d}\boldsymbol{k} \\ &= \left|\int H(\boldsymbol{k})\,\frac{1}{k_0}\exp(2i\boldsymbol{k}\boldsymbol{r}_0)\,\phi^*\left(\frac{1}{k_0}[\boldsymbol{R}]_{\theta_0}^{-1}\boldsymbol{k}\right)\mathrm{d}\boldsymbol{k}\right|^2 \end{aligned} \quad (14)$$

The right-hand side of (14) is the wavelet coefficient $F(\boldsymbol{r}_0, \boldsymbol{k}_0)$, defined as the scalar product between the reflected signal H and each element $\Psi_{\boldsymbol{r}_0,\boldsymbol{k}_0}$ of the wavelet basis

$$\begin{aligned} F(\boldsymbol{r}_0, \boldsymbol{k}_0) &= \int H(\boldsymbol{k})\,\Psi_{\boldsymbol{r}_0,\boldsymbol{k}_0}^*(\boldsymbol{k})\,\mathrm{d}\boldsymbol{k} \\ &= \int_0^{2\pi}\mathrm{d}\theta\int_0^{+\infty} k\,H(k, \theta)\,\Psi_{\boldsymbol{r}_0,\boldsymbol{k}_0}^*(\boldsymbol{k})\,\mathrm{d}k \end{aligned} \quad (15)$$

One may note that the wavelet coefficient is invariant by any transformation of the $\mathcal{S}$ group.

The reconstruction property allows one to recover the signal from its wavelet coefficients as

$$H(\boldsymbol{k}) = \frac{1}{K(\phi)}\int \mathrm{d}\boldsymbol{r}_0 \int F(\boldsymbol{r}_0, \boldsymbol{k}_0)\,\Psi_{\boldsymbol{r}_0,\boldsymbol{k}_0}(\boldsymbol{k})\,\mathrm{d}\boldsymbol{k}_0 \quad (16)$$

where $K(\phi)$ is the admissibility coefficient given by

$$K(\phi) = \int \frac{|\phi(\boldsymbol{k})|^2}{k^2}\,\mathrm{d}\boldsymbol{k} < +\infty \quad (17)$$

From (4), (14) and (15), one can conclude that the wavelet coefficient $F(\boldsymbol{r}_0, \boldsymbol{k}_0)$ is equal to the coherent complex image $S(\boldsymbol{r}_0, \boldsymbol{k}_0)$

$$F(\boldsymbol{r}_0, \boldsymbol{k}_0) = S(\boldsymbol{r}_0, \boldsymbol{k}_0) \quad (18)$$

3.3 Interpretation of the distribution $I(\boldsymbol{r}, \boldsymbol{k})$

Rewriting $I(\boldsymbol{r}, \boldsymbol{k})$ as $I(x, y, f, \theta)$ shows that for each frequency f_0 and each angle of radar illumination θ_0, $I(x, y, f_0, \theta_0)$ represents a spatial distribution of the backscattered energy for this frequency and angle.

Reciprocally, for a given spatial location, $\boldsymbol{r}_0 = (x_0, y_0)^{\mathrm{T}}$, $I(x_0, y_0, f, \theta)$ provides the 2-D spectral behaviour of the corresponding scatterer.

To analyse this 4D structure, a visual display interface called i4D has been developed and allows one to carry out an interactive and dynamic analysis.

3.4 Other multidimensional TF transforms

The hyper-image concept can be generalised to all TF transforms [10], like the smoothed pseudo Wigner–Ville transform used to detect targets in [11]. However, TF techniques dealing with polarimetric data need preserve the relative phase information between the polarimetric channels. This coherent constraint is only verified by atomic decompositions, like the short time Fourier transform (STFT) and the continuous wavelet transform. Some examples of TF processing of polarimetric SAR data using the STFT can be found in [12] and [13]. In this study, the continuous wavelet transform is preferred since its covariance property is better adapted to the analysis of anechoic chamber measurements [5].

Moreover, the proposed TF technique, as a particular case of atomic decompositions (wavelet and STFT), decomposes the UWB signal into 2-D sub-spectra that can be interpreted as frequency sub-bands and angular sub-sectors.

It is not the case of other TF approaches, like in particular quadratic distributions (Wigner–Ville, smoothed pseudo Wigner–Ville, the Choi–Williams distribution, the Born–Jordan, Page or Rihaczek distributions). Indeed, these distributions may achieve higher performance (resolution, ...) that can be used to detect and locate particular signals (chirps, ...) but as the expense of physical interpretation (they might be real-valued, non-positive, have pseudo energy, ...).

Anyway, as it uses atomic decompositions, the approach presented in this paper relies on strong physical considerations. The use of wavelets or STFT is simply a matter of representation and does not violate the physical considerations radar imaging is based on.

3.5 Polarimetric generalisation of the hyper-image concept

The wavelet transform defined in (15) is applied in a similar way to each of the four polarimetric channels mentioned in (5). The resulting scattering matrix is a multivariate function of the frequency and on the illumination angle and is called hyper-scattering matrix

$$\boldsymbol{S}(\boldsymbol{r}, \boldsymbol{k}) = \begin{bmatrix} S_{hh}(\boldsymbol{r}, \boldsymbol{k}) & S_{hv}(\boldsymbol{r}, \boldsymbol{k}) \\ S_{vh}(\boldsymbol{r}, \boldsymbol{k}) & S_{vv}(\boldsymbol{r}, \boldsymbol{k}) \end{bmatrix} \quad (19)$$

Due to the use of a phase preserving TF transform the hyper-scattering matrix given in (19) can be analysed and interpreted using traditional polarimetric approaches.

Similarly to the classical polarimetric span, the extended span is defined as the sum of the squared modulus of each

doi: 10.1049/iet-rsn.2008.0086

element of the hyper-scattering matrix (19).

$$P(\boldsymbol{r}, \boldsymbol{k}) = |S_{hh}(\boldsymbol{r}, \boldsymbol{k})|^2 + |S_{hv}(\boldsymbol{r}, \boldsymbol{k})|^2 + |S_{vh}(\boldsymbol{r}, \boldsymbol{k})|^2 + |S_{vv}(\boldsymbol{r}, \boldsymbol{k})|^2 \tag{20}$$

The extended span does not represent the whole extended polarimetric information, but is a basic representation of the energetic polarimetric behaviour in both space and spectral domains.

The proposed approach is applied to fully polarimetric measurements acquired in an anechoic chamber. The observed target is a 'Cyrano' weapon scaled model, made out of steel (length 1.2 m – width 0.60 m) and represented on Fig. 1. Backscattering coefficients are measured over a frequency band ranging from 12 up to 18 GHz, with a sampling rate of 0.75 MHz, and for an azimuthal orientation varying from -25 to $+25°$ with 0.5° increments. The evolution of the extended span as a function of the emitted frequency and the observation angle is represented on Fig. 2. In the following, scatterers of interest, whose location is indicated on Fig. 2, are selected and their TF behaviour is described.

- *Head (P1):* The response of the weapon model's head is characterised by a non-dispersive and isotropic behaviour.

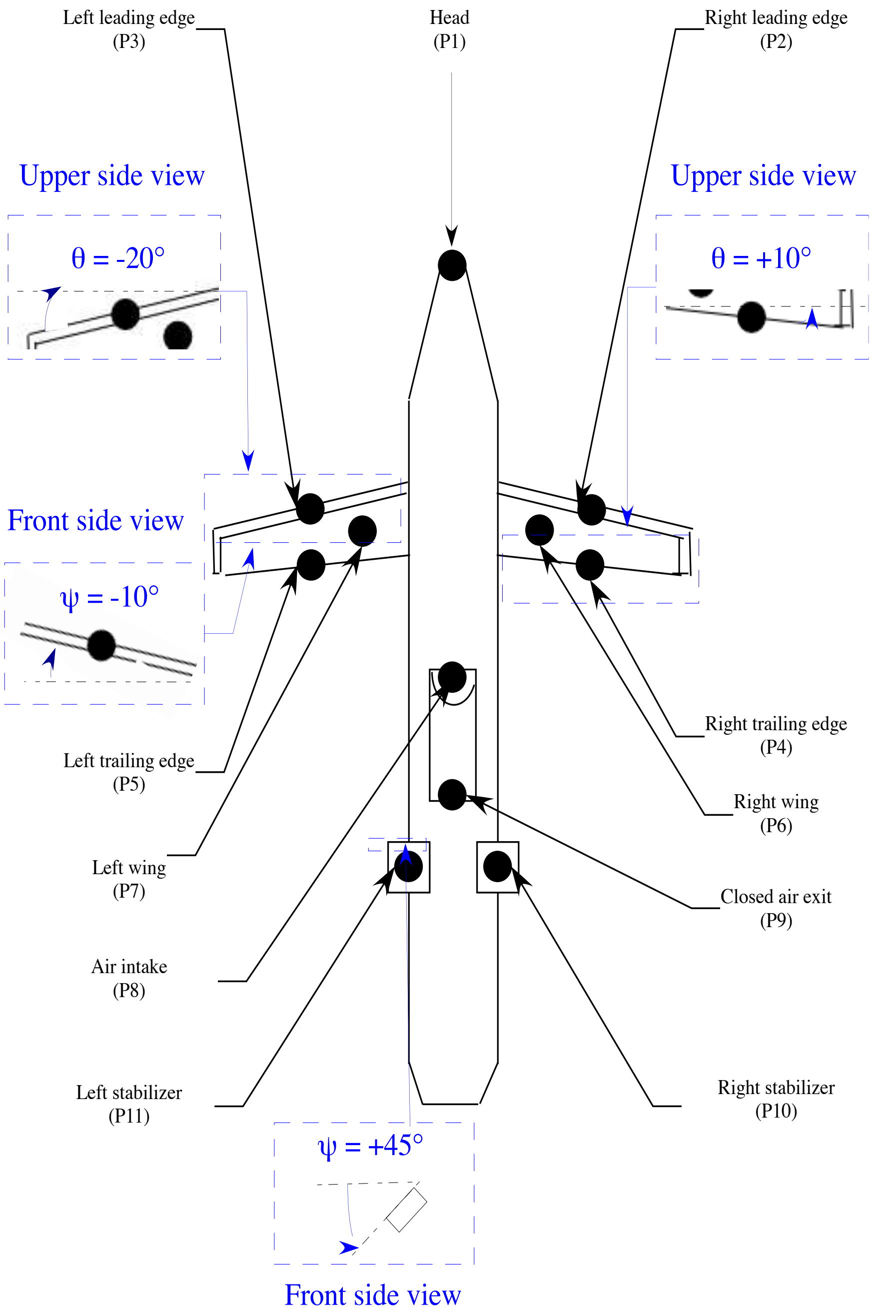

Figure 1 *Cyrano weapon model*

doi: 10.1049/iet-rsn.2008.0086

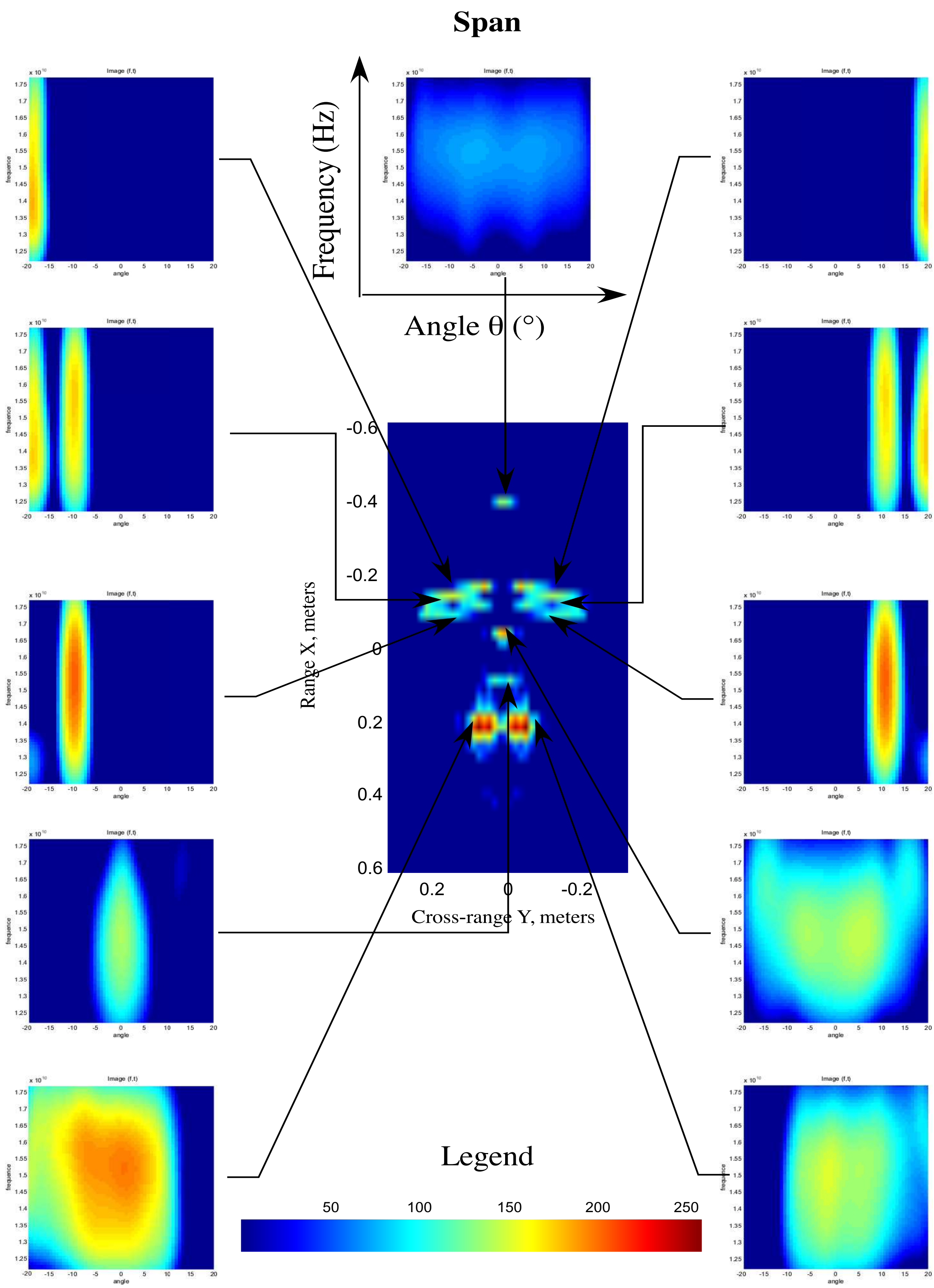

Figure 2 *Extended span over selected locations*

IET Radar Sonar Navig., pp. 1–19
doi: 10.1049/iet-rsn.2008.0086

This stationary behaviour is due to the particular geometry of the head, whose shape is a semi-sphere known to reflect electromagnetic waves in an isotropic and non-dispersive way over the angular-frequency domain used for this experiment.

- *Leading edges (P2, P3):* Leading edges are identified by a directional response in the angle–frequency domain. The aspect angle corresponding to the maximum of the backscattered energy, $\theta = \pm 20^\circ$, indicates the orientation of the wing edges with respect to the radar beam. As explained in [14] this directional behaviour expresses a diffraction phenomenon.

- *Trailing edges (P4, P5):* Similarly to leading edges, trailing edges have a directional behaviour in the angle–frequency plane, due to wave diffraction as well [14]. The backscattered energy reaches a maximum for an angle of view of $\theta = \pm 10^\circ$, which exactly corresponds to the orientation of this part of the illuminated object with respect to the horizontal to the radar beam.

- *Wings (P6, P7):* These particular points demonstrate a limitation of the proposed TF analysis approach, known as the Heisenberg uncertainty principle, inherent to the kind of TF transform used in this study. Indeed, the resolution of a joint TF analysis using continuous wavelets is limited by the Heisenberg inequality, which provides a physical lower bound for the product of the spatial and spectral resolutions. As a consequence, for a given spectral resolution, the TF responses of too closely spaced scatterers cannot be discriminated. This resolution trade-off phenomenon is well illustrated over the wings, whose angle–frequency response presents two directional features ($\theta = \pm 10^\circ$ and $\theta = \pm 20^\circ$), corresponding to artefacts generated by the leading and trailing edges as presented above.

  This case highlights potential limitations, in terms of signal separation, of the proposed hyper-image approach.

- *Air intake (P8):* The air intake response appears as dispersive and anisotropic, indicating the presence of complex scattering mechanisms that are highly dependent on the conditions of acquisition.

- *Closed air exit (P9):* The 2-D characteristic of the close air exit is highly directive and is centred around $\theta = 0^\circ$. This behaviour is due to the specular reflection of the emitted signal over the closed air exit, which occurs as the radar faces the exit, that is when the air exit behaves as a waveguide.

- *Stabilisers (P10, P11):* These responses do not show any particular angular of frequency behaviours. One may note that the geometrical symmetry between the left and right stabilisers can be observed from their 2-D characteristics.

As shown by the results depicted in Fig. 2, the extended span permits one to highlight scatterers with an anisotropic or dispersive polarimetric energetic response and may be used to investigate local scattering phenomena, in terms of scattering mechanisms and orientation with respect to the radar beam. In order to characterise the degree of anisotropy and dispersion of the extended span, one can compute the marginal densities in the frequency and angular domains as

$$P_f(\boldsymbol{r}, f) = \frac{\int_\theta P(\boldsymbol{r}, \boldsymbol{k})\,\mathrm{d}\theta}{\int P(\boldsymbol{r}, \boldsymbol{k})\,\mathrm{d}\boldsymbol{k}} \tag{21}$$

and

$$P_\theta(\boldsymbol{r}, \theta) = \frac{\int_k k\,P(\boldsymbol{r}, \boldsymbol{k})\,\mathrm{d}k}{\int P(\boldsymbol{r}, \boldsymbol{k})\,\mathrm{d}\boldsymbol{k}} \tag{22}$$

Frequency and angular marginal densities of the extended span, computed over particular locations of the Cyrano weapon, are represented in Figs. 3 and 4. The marginal densities in frequency indicate that all the selected points are affected by a similar dispersive behaviour, characterised by a Gaussian-like shape and centered around the mean frequency. It is likely that this pattern corresponds to the frequency response of the radar device itself and not to a frequency-sensitive target response. The marginal densities in angle relate very well the sensitivity of the response of some of the target elements to this parameter, as explained above.

The extended span and its marginal densities are basic tools that may be used to roughly characterise the polarimetric TF behaviour of an object. Indeed, the span is a global energetic indicator, but does not account for phase and amplitude imbalances between the polarimetric channels, and other polarimetric approaches, like the decomposition into scattering mechanisms, might be used to refine the analysis of the target polarimetric response. Among the wide variety of polarimetric decomposition approaches, the so-called coherent decompositions, applying directly onto scattering matrices, are particularly well adapted to the study of high-resolution anechoic chamber measurements of deterministic targets that are not affected by incoherent perturbations from natural environments. Due to the phase preservation property of the selected TF transform, coherent polarimetric decomposition techniques can be directly applied onto hyper-scattering matrices. The most popular coherent polarimetric decomposition schemes are presented in the following section.

4 Coherent polarimetric decompositions

4.1 Pauli decomposition

The Pauli decomposition expresses the measured scattering matrix $\boldsymbol{S}$ in a modified Pauli basis [15], given by the

doi: 10.1049/iet-rsn.2008.0086

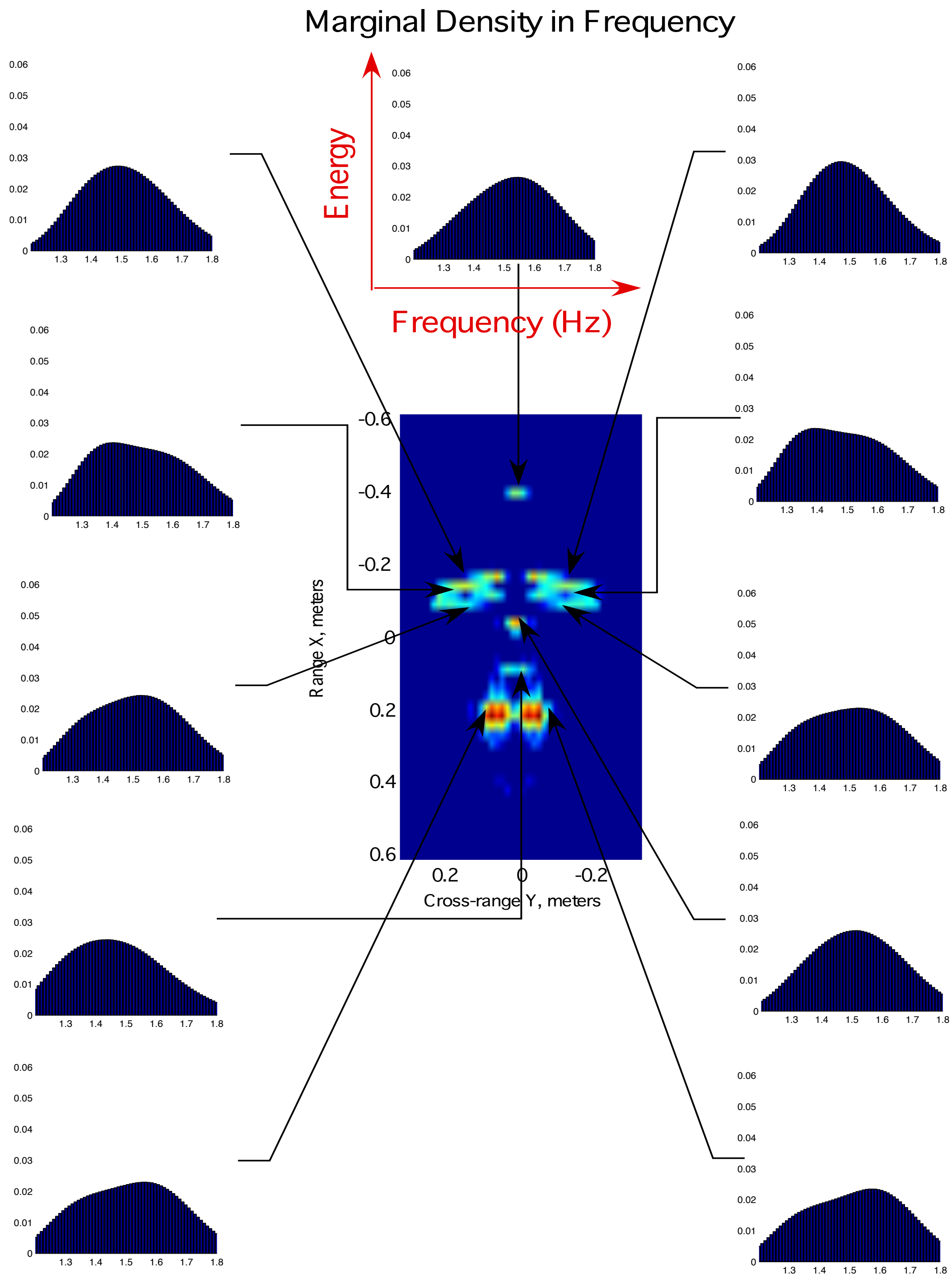

Figure 3 *Extended span marginal density in frequency*

following four matrices

$$S_a = \frac{1}{\sqrt{2}}\begin{bmatrix} 1 & 0 \\ 0 & 1 \end{bmatrix} \tag{23}$$

$$S_b = \frac{1}{\sqrt{2}}\begin{bmatrix} 1 & 0 \\ 0 & -1 \end{bmatrix} \tag{24}$$

$$S_c = \frac{1}{\sqrt{2}}\begin{bmatrix} 0 & 1 \\ 1 & 0 \end{bmatrix} \tag{25}$$

$$S_d = \frac{1}{\sqrt{2}}\begin{bmatrix} 0 & -1 \\ 1 & 0 \end{bmatrix} \tag{26}$$

In a monostatic system configuration, the reciprocity principle $S_{hv} = S_{vh}$ applies, and the modified Pauli basis can be reduced to S_a, S_b and S_c. Consequently, a symmetric scattering matrix S can be expressed as

$$S = \begin{bmatrix} S_{hh} & S_{hv} \\ S_{hv} & S_{vv} \end{bmatrix} = \alpha\, S_a + \beta\, S_b + \gamma\, S_c \tag{27}$$

doi: 10.1049/iet-rsn.2008.0086

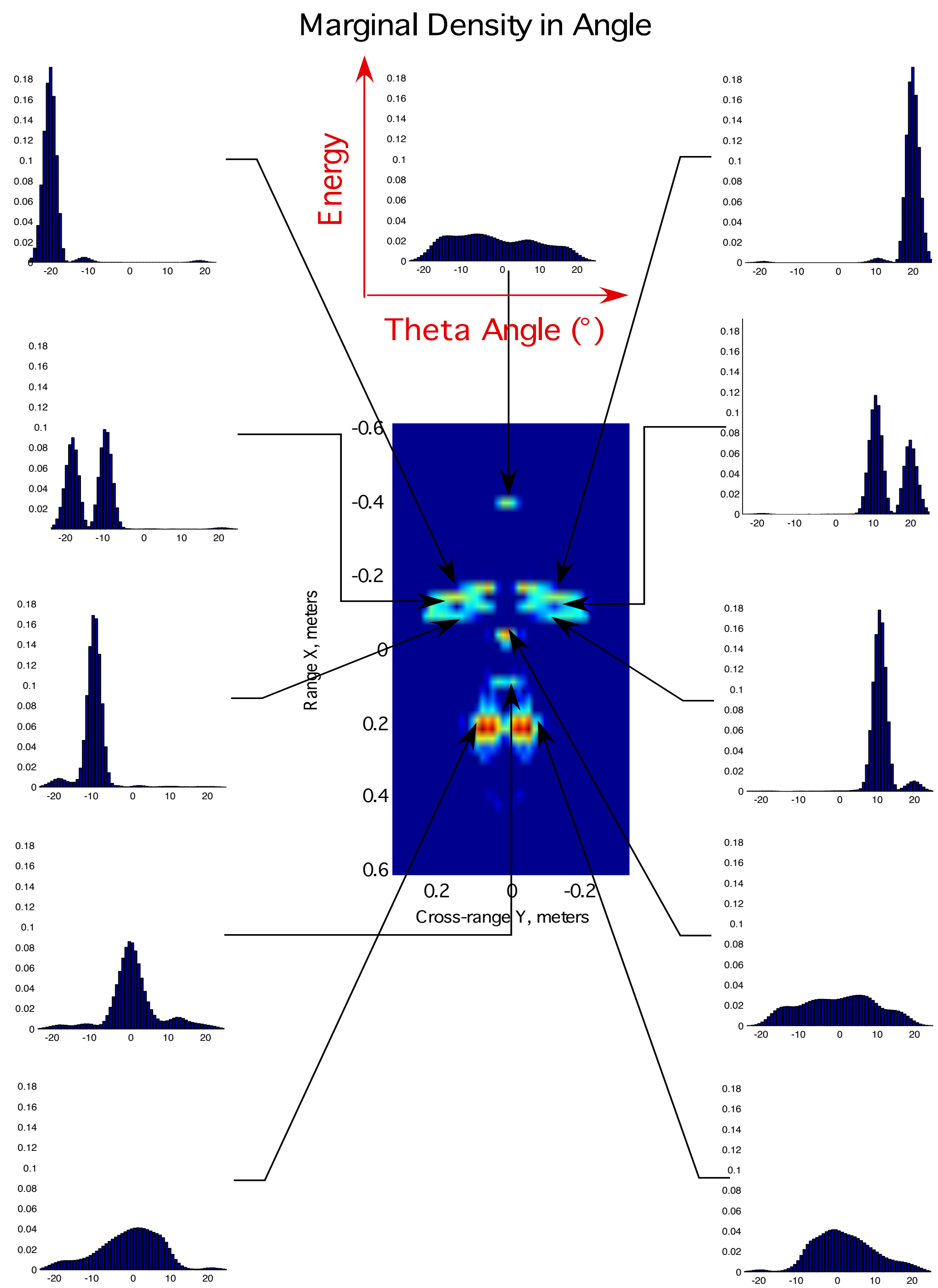

Figure 4 *Extended span marginal density in angle*

where the complex coefficients α, β, γ are given by

$$\alpha = \frac{S_{hh} + S_{vv}}{\sqrt{2}}, \quad \beta = \frac{S_{hh} - S_{vv}}{\sqrt{2}}, \quad \gamma = \sqrt{2}S_{hv} \tag{28}$$

The span can be obtained from the decomposition coefficients α, β, γ, as

$$P = |\alpha|^2 + |\beta|^2 + |\gamma|^2 \tag{29}$$

This polarimetric processing approach decomposes a scattering matrix into components associated to orthogonal canonical scattering mechanisms. The term $\boldsymbol{S}_a$ represents the response of a plate observed at normal incidence or a sphere, whereas $\boldsymbol{S}_b$ is characteristic of a horizontal metallic dihedral. The last component $\boldsymbol{S}_c$ represents the scattering matrix of a metallic dihedral oriented at 45° with respect to the radar line of sight.

The squared modulus of the decomposition coefficients $|\alpha|^2, |\beta|^2, |\gamma|^2$, represents the amount of the scattered energy that can be associated to each of the canonical scattering mechanism.

4.2 Krogager decomposition

A more refined alternative approach, proposed by E. Krogager [16–18] and considering a scattering matrix as the combination of the responses of a sphere, an oriented diplane and a helix, can be formulated as

$$\boldsymbol{S} = \mathrm{e}^{\mathrm{j}\varphi}\{\mathrm{e}^{\mathrm{j}\varphi_s}\, k_s\, \boldsymbol{S}_{\text{sphere}} + k_d\, \boldsymbol{S}_{\text{diplane}}(\vartheta) + k_h\, \boldsymbol{S}_{\text{helix}}(\vartheta)\} \tag{30}$$

with

$$\boldsymbol{S}_{\text{sphere}} = \begin{bmatrix} 1 & 0 \\ 0 & 1 \end{bmatrix},\ \boldsymbol{S}_{\text{diplane}}(\vartheta) = \begin{bmatrix} \cos 2\vartheta & \sin 2\vartheta \\ \sin 2\vartheta & -\cos 2\vartheta \end{bmatrix}$$
$$\boldsymbol{S}_{\text{helix}}(\vartheta) = \mathrm{e}^{(\pm 2\mathrm{j}\vartheta)}\begin{bmatrix} 1 & \pm\mathrm{j} \\ \pm\mathrm{j} & -1 \end{bmatrix} \tag{31}$$

where the $\pm$ sign in the helix component varies its the handedness, left or right, and has to be fixed during the estimation of the decomposition components. The identification of the parameters introduced in (30) and (31) is generally performed in the right–left circular basis, where the expression of the scattering matrix is

$$\boldsymbol{S}_{(r,l)} = \begin{bmatrix} S_{rr} & S_{rl} \\ S_{rl} & S_{ll} \end{bmatrix} = \begin{bmatrix} |S_{rr}|\,\mathrm{e}^{\mathrm{j}\varphi_{rr}} & |S_{rl}|\,\mathrm{e}^{\mathrm{j}\varphi_{rl}} \\ |S_{rl}|\,\mathrm{e}^{\mathrm{j}\varphi_{rl}} & -|S_{ll}|\,\mathrm{e}^{\mathrm{j}(\varphi_{ll}+\pi)} \end{bmatrix} \tag{32}$$

with

$$S_{rr} = \mathrm{j}S_{hv} + \frac{1}{2}(S_{hh} - S_{vv}),\quad S_{ll} = \mathrm{j}S_{hv} - \frac{1}{2}(S_{hh} - S_{vv})$$
$$S_{rl} = \frac{\mathrm{j}}{2}(S_{hh} + S_{vv}) \tag{33}$$

The decomposition may then be formulated as

$$\boldsymbol{S}_{(r,l)} = \mathrm{e}^{\mathrm{j}\varphi}\left\{\mathrm{e}^{\mathrm{j}\varphi_s}\, k_s \begin{bmatrix} 0 & \mathrm{j} \\ \mathrm{j} & 0 \end{bmatrix} + k_d \begin{bmatrix} \mathrm{e}^{\mathrm{j}2\vartheta} & 0 \\ 0 & -\mathrm{e}^{-\mathrm{j}2\vartheta} \end{bmatrix} + k_h \begin{bmatrix} \mathrm{e}^{\mathrm{j}2\vartheta} & 0 \\ 0 & 0 \end{bmatrix}\right\} \tag{34}$$

from which parameters can be estimated as follows

$$\begin{cases} \varphi = \frac{1}{2}(\varphi_{rr} + \varphi_{ll} - \pi) \\ \vartheta = \frac{1}{4}(\varphi_{rr} - \varphi_{ll} + \pi) \\ \varphi_s = \varphi_{rl} - \frac{1}{2}(\varphi_{rr} + \varphi_{ll}) \end{cases} \tag{35}$$
$$\begin{cases} k_s = |S_{rl}|, \\ k_d = |S_{ll}|, \quad k_h = |S_{rr}| - |S_{ll}| \quad \text{if } |S_{rr}| > |S_{ll}| \\ k_d = |S_{rr}|, \quad k_h = |S_{ll}| - |S_{rr}| \quad \text{otherwise} \end{cases}$$

where the condition $|S_{rr}| > |S_{ll}|$ denotes the presence of a left-handed helix contribution. The absolute phase φ is fixed by the acquisition geometry and calibration and does not contain any relevant polarimetric information. The remaining five parameters, φ_s, k_s, k_d, k_h and ϑ, can be associated to physical properties of the target. The term φ_s is proportional to the path travelled by the radar signal between the phase centres of the sphere and diplane/helix contributions. The parameter ϑ stands for the orientation angle of the diplane and the helix scattering mechanisms around the radar line of sight. The coefficients k_s, k_d and k_h represent the amplitude of each canonical scattering mechanisms contributing to the originally measured scattering matrix $\boldsymbol{S}$.

4.3 Cameron decomposition

4.3.1 Principle of polarimetric symmetry: A scattering matrix may be represented under the form of a complex four-element scattering vector as

$$\boldsymbol{k_S} = [S_{hh}, S_{hv}, S_{vh}, S_{vv}]^{\mathrm{T}} \tag{36}$$

For reciprocal scattering responses, $S_{hv} = S_{vh}$, the decomposition of a scattering vector on the modified Pauli basis vector set may be written from (27) as

$$\boldsymbol{k_S} = \alpha\,\boldsymbol{k}_{\boldsymbol{S}_a} + \beta\,\boldsymbol{k}_{\boldsymbol{S}_b} + \gamma\,\boldsymbol{k}_{\boldsymbol{S}_c} \tag{37}$$

where each coefficient of the decomposition is obtained by projecting the scattering vector $\boldsymbol{k_S}$ onto each element of the orthonormal Pauli vector set, for example $\alpha = \boldsymbol{k}_{\boldsymbol{S}}^{\mathrm{T}}\boldsymbol{k}_{\boldsymbol{S}_a}$.

A scattering mechanism is considered as symmetric if the projection of its scattering vector onto the cross-polarised component of the Pauli basis, $\boldsymbol{k}_{\boldsymbol{S}_c}$, can be nullified by rotating the polarisation basis around the radar line of sight [19, 20]. Such a scattering vector may then be written as

$$\boldsymbol{k}_{\boldsymbol{S}_{\text{sym}}} = a\,\mathrm{e}^{\mathrm{i}\rho}\,\boldsymbol{R}_{\psi}\,\boldsymbol{\lambda}(z),\ \text{with}\ \boldsymbol{\lambda}(z) = \frac{1}{\sqrt{1+|z|^2}}[1, 0, 0, z]^{\mathrm{T}} \tag{38}$$

where $\boldsymbol{\lambda}(z)$ is a scattering vector satisfying $\boldsymbol{\lambda}^{\mathrm{T}}(z)\boldsymbol{k}_{\boldsymbol{S}_c} = 0$, parametrised by the complex valued scalar z, a is the

doi: 10.1049/iet-rsn.2008.0086

amplitude of the scattering matrix, ρ is the absolute phase, and $\boldsymbol{R}_\psi$ is a rotation matrix given by

$$\boldsymbol{R}_\psi = \boldsymbol{R}_2(\psi) \otimes \boldsymbol{R}_2(\psi), \text{ with } \boldsymbol{R}_2(\psi) = \begin{bmatrix} \cos\psi & -\sin\psi \\ \sin\psi & \cos\psi \end{bmatrix} \tag{39}$$

where ψ represents the angle of rotation and $\otimes$ the Kronecker product.

A symmetric scattering mechanisms corresponds to a target having an axis of symmetry around the radar line of sight, whose orientation, often called the Huynen orientation, is given by ψ. Examples of normalised scattering vectors corresponding to symmetric canonical scattering mechanisms are given in Table 1.

4.3.2 Decomposition into canonical scattering mechanisms: A reciprocal scattering vector can be decomposed as a weighted sum of two symmetric orthogonal scattering components [19, 20], as

$$\boldsymbol{k}_S = \cos\tau\, \boldsymbol{k}_{S^{\text{sym}}_{\text{max}}} + \sin\tau\, \boldsymbol{k}_{S^{\text{sym}}_{\text{min}}} \tag{40}$$

The angle τ represents the degree to which the scattering vector deviates from being symmetric

$$\cos\tau = \frac{|\boldsymbol{k}_S^{\mathrm{T}} \boldsymbol{k}_{S^{\text{sym}}_{\text{max}}}|}{|\boldsymbol{k}_S|\,|\boldsymbol{k}_{S^{\text{sym}}_{\text{max}}}|} \quad 0 \le \tau \le \frac{\pi}{4} \tag{41}$$

A scattering mechanism with $\tau = 0$ represents a fully symmetric scatterer like a trihedral or a dihedral, whereas a scattering matrix with $\tau = \pi/4$ represents a fully asymmetric scatterer, like a left or right-handed helix.

The symmetric scattering vectors $\boldsymbol{k}_{S^{\text{sym}}_{\text{max}}}$ and $\boldsymbol{k}_{S^{\text{sym}}_{\text{min}}}$ are given by

$$\boldsymbol{k}_{S^{\text{sym}}_{\text{min}}} = \alpha\, \boldsymbol{k}_{S_a} + \varepsilon\, \boldsymbol{k}_{S_b}, \quad \boldsymbol{k}^{\mathrm{T}}_{S^{\text{sym}}_{\text{max}}} \boldsymbol{k}_{S^{\text{sym}}_{\text{min}}} = 0 \tag{42}$$

Table 1 Examples of normalised vectors associated to canonical symmetric scatterers

Symmetric scatterer	Normalised vector
trihedral	$\boldsymbol{\lambda}(1)$
diplane	$\boldsymbol{\lambda}(-1)$
dipole	$\boldsymbol{\lambda}(0)$
cylinder	$\boldsymbol{\lambda}(1/2)$
narrow diplane	$\boldsymbol{\lambda}(-1/2)$
quarter wave device	$\boldsymbol{\lambda}(i)$

where ε is given by

$$\varepsilon = \beta\cos(\xi) + \gamma\sin(\xi), \qquad \tan(2\xi) = \frac{\beta\gamma^* + \beta^*\gamma}{|\beta|^2 - |\gamma|^2} \tag{43}$$

The minimum and maximum attributes of the symmetric scattering vectors refer to the relative amplitude of their contribution to $\boldsymbol{k}_S$, steered by τ, which by construction verifies $\cos\tau \ge \sin\tau$. The orientation of the target is generally estimated from the representation of $\boldsymbol{k}_{S^{\text{max}}_{\text{min}}}$ under the form shown in (38).

Based on the decomposition of the measured scattering matrix $\boldsymbol{S}$ into symmetric components, Cameron proposed a classification scheme described on Fig. 5 [19, 20]. The initial test of reciprocity is verified in the monostatic acquisition configuration of this study. The input scattering matrix is then decomposed using (40), (42) and (43). The characteristic parameter τ is used to estimate the degree of symmetry of the input matrix: if $\tau \le \pi/8$ the scatterer is considered as mainly symmetric, whereas for $\tau > \pi/8$ it is associated to an non-symmetric object or a helix if $\tau \simeq \pi/4$. Scatterers labelled as symmetric may be further characterised using the decomposition of $\boldsymbol{k}_{S^{\text{sym}}_{\text{max}}}$ shown in (38). The complex parameter z is compared to those of the reference canonical targets shown in Table 1, that is trihedral, dihedral, dipole, cylinder, narrow-diplane and quarter wave device. The scatterer under observation is assigned to the class of the reference canonical response

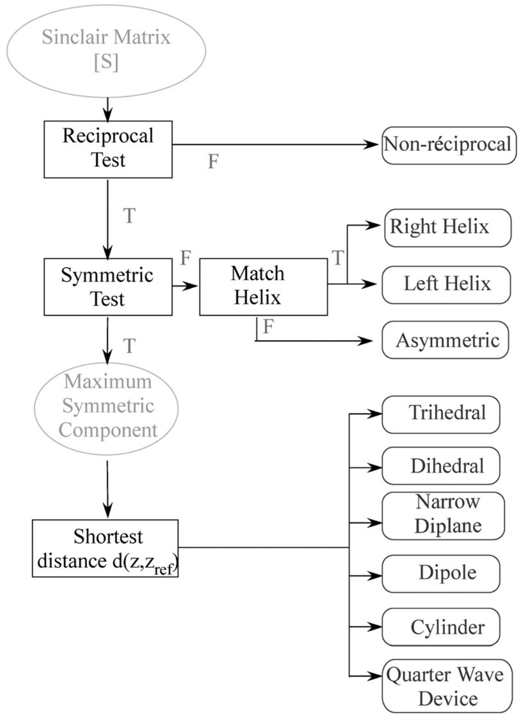

Figure 5 *Classification process of the Cameron decomposition*

minimising the following metric

$$d(z, z_{\text{ref}}) = \cos^{-1}\left(\frac{\max(|1 + z\, z_{\text{ref}}^*|, |z + z_{\text{ref}}^*|)}{\sqrt{1+|z|^2}\sqrt{1+|z_{\text{ref}}|^2}}\right) \quad (44)$$

5 Polarimetric TF analysis using coherent decompositions

5.1 Polarimetric decomposition of hyper-images

As mentioned in Section 3.5, hyper-scattering matrices may be obtained by simultaneously applying a phase preserving TF transform over each polarisation channel. The resulting multidimensional information may then be analysed through polarimetric coherent decompositions in order to generate hyper-images of relevant parameters, that is images representing values taken by these parameters over the measured frequency and observation angle domains, as introduced in [21, 22].

The Krogager decomposition of a hyper-scattering matrix may be written as

$$\begin{aligned} \boldsymbol{S}(\boldsymbol{r}, \boldsymbol{k}) = \mathrm{e}^{\mathrm{i}\varphi(\boldsymbol{r},\boldsymbol{k})}\{\mathrm{e}^{\mathrm{i}\varphi_s(\boldsymbol{r},\boldsymbol{k})} k_s(\boldsymbol{r}, \boldsymbol{k})\, \boldsymbol{S}_{\text{sphere}} + k_d(\boldsymbol{r}, \boldsymbol{k})\, \boldsymbol{S}_{\text{diplane}}(\vartheta(\boldsymbol{r}, \boldsymbol{k})) \\ + k_h(\boldsymbol{r}, \boldsymbol{k})\, \boldsymbol{S}_{\text{helix}}(\vartheta(\boldsymbol{r}, \boldsymbol{k}))\} \quad (45) \end{aligned}$$

where the most significant hyper-images are given by $|k_s(\boldsymbol{r}, \boldsymbol{k})|^2$, $|k_d(\boldsymbol{r}, \boldsymbol{k})|^2$, $|k_h(\boldsymbol{r}, \boldsymbol{k})|^2$, the intensity associated to the sphere, diplane and helix components, respectively, and $\vartheta(\boldsymbol{r}, \boldsymbol{k})$, the orientation angle of the diplane and helix components.

The decomposition of a reciprocal hyper-scattering matrix using Cameron's approach leads to

$$\boldsymbol{S}(\boldsymbol{r}, \boldsymbol{k}) = \cos \tau(\boldsymbol{r}, \boldsymbol{k})\, \boldsymbol{S}_{\text{sym}}^{\max}(\boldsymbol{r}, \boldsymbol{k}) + \sin \tau(\boldsymbol{r}, \boldsymbol{k})\, \boldsymbol{S}_{\text{sym}}^{\min}(\boldsymbol{r}, \boldsymbol{k}) \quad (46)$$

The most significant parameters obtained from this decomposition approach are the classification into canonical scattering mechanisms, $W(\boldsymbol{r}, \boldsymbol{k})$, the Huynen orientation $\psi(\boldsymbol{r}, \boldsymbol{k})$, and the measure of symmetry $\tau(\boldsymbol{r}, \boldsymbol{k})$.

5.2 Experimental results

The proposed polarimetric hyper-images processing techniques are applied to the anechoic chamber measurements of the Cyrano weapon model described in Section 3.5. Results obtained using the Krogager decomposition are shown in Fig. 6 under the form of colour-coded images, computed from the intensity of the sphere, diplane and helix components. Hyper-images of the classification map and Huynen oriental angle, obtained using the Cameron decomposition are depicted in Figs. 7 and 8, respectively. In order to avoid meaningless classification results, the representation of the parameters derived from the Cameron decomposition is limited to frequency and angular domains corresponding to significant extended span values.

The analysis of TF parameters derived from both polarimetric decomposition approaches is discussed in the following over the particular locations indicated in Fig. 2.

- *Head (P1):* Both decompositions indicate a stationary TF polarimetric behaviour. The polarimetric behaviour of the weapon model's head is stationary. The dominant scattering behaviour is identified as a canonical sphere or trihedral reflector response, both characterised by a single bounce reflection of the electromagnetic wave by this part of the object. This constant polarimetric patterns observed at this spatial location is conferred by the geometrical shape of the head as explained during the analysis of the extended span.

- *Leading edges (P2, P3):* These parts of the object show a very directional response, mainly driven by the span, with a peak of the backscattered energy, centred on the horizontal orientation of the edges, that is $\theta = \pm 20^\circ$. The Krogager decomposition identifies the corresponding polarimetric response as a mixture of sphere and diplane contributions, whereas the Cameron approach more accurately classifies these narrow and anisotropic scatterers as dipoles. The Huynen orientation provides a precise estimate of the orientation of the wings with the radar line of sight, $\psi = \pm 10^\circ$. One may note the non-dispersive behaviour of the extended span and other extended polarimetric indicators. The edges clearly illustrate the potential of a polarimetric TF analysis to deeply characterise an object in terms of canonical scattering mechanism and relative orientation with respect to both horizontal and vertical planes.

- *Trailing edges (P4, P5):* A similar polarimetric behaviour is observed over the trailing edges. The horizontal orientation is well estimated with $\theta = \pm 10^\circ$. The poor estimation, $\psi = \pm 90^\circ$, of the vertical orientation is due to the fact that radar does not see the slope (upper view).

- *Wings (P6, P7):* The effects of the time and frequency-limited resolutions, linked to the Heisenberg uncertainty principle introduced earlier in this paper, are clearly visible on the TF polarimetric hyper-images, the TF behaviour of the wings being indeed a mixture of the polarimetric patterns of the leading and trailing wings.

- *Air intake (P8):* The polarimetric indicators confirm the dispersive and anisotropic behaviours observed during the analysis of the extended span, that are probably linked to the geometrical complexity of this scatterer.

doi: 10.1049/iet-rsn.2008.0086

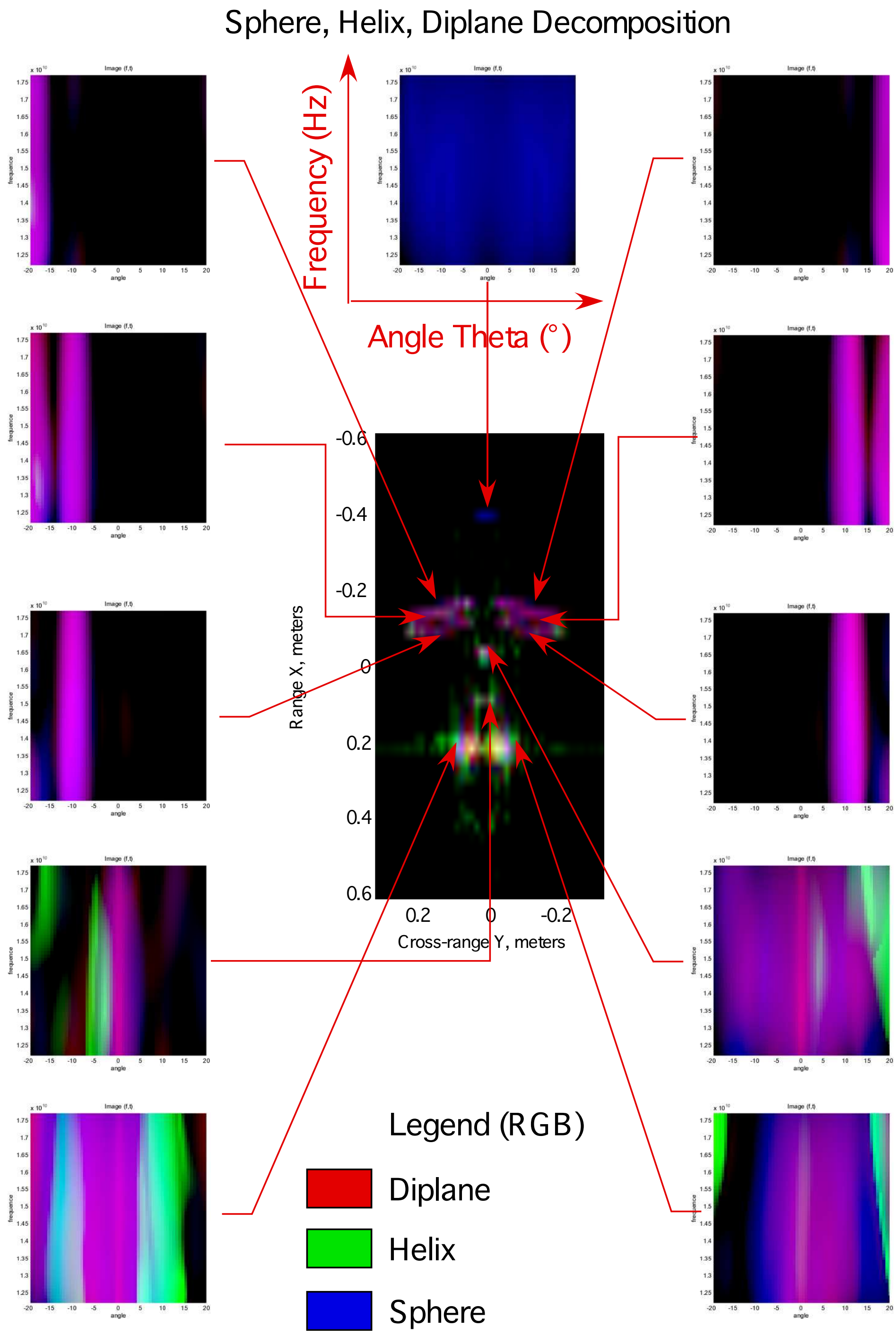

Figure 6 *Colour-coded hyper-images of the Krogager decomposition amplitude coefficients*

- *Closed air exit (P9):* The indicators derived from the Krogager and Cameron decompositions depict relate well the highly directive behaviour of the closed air exit centred on $\theta = 0^\circ$. The non-stationary aspect of the polarimetric features indicates that the scattering mechanism may not be a specular reflection over the closed exit, as previously presented during the analysis of the extended span, but a more complicated combination of scattering modes.

- *Stabilisers (P10, P11):* Similarly to the extended span, polarimetric decomposition parameters show a quasi-perfect symmetry between right and left wings. The hyper-images show that the TF scattering mechanism is clearly a function of the observation angle θ. This non-stationary behaviour is due to the strong variations of the slant range geometry as the aspect angle varies: the horizontal, $\theta \simeq 0^\circ$, dipole contribution with a Huynen orientation $\psi = \pm 45^\circ$ is caused by the edge of the stabiliser, whereas, as

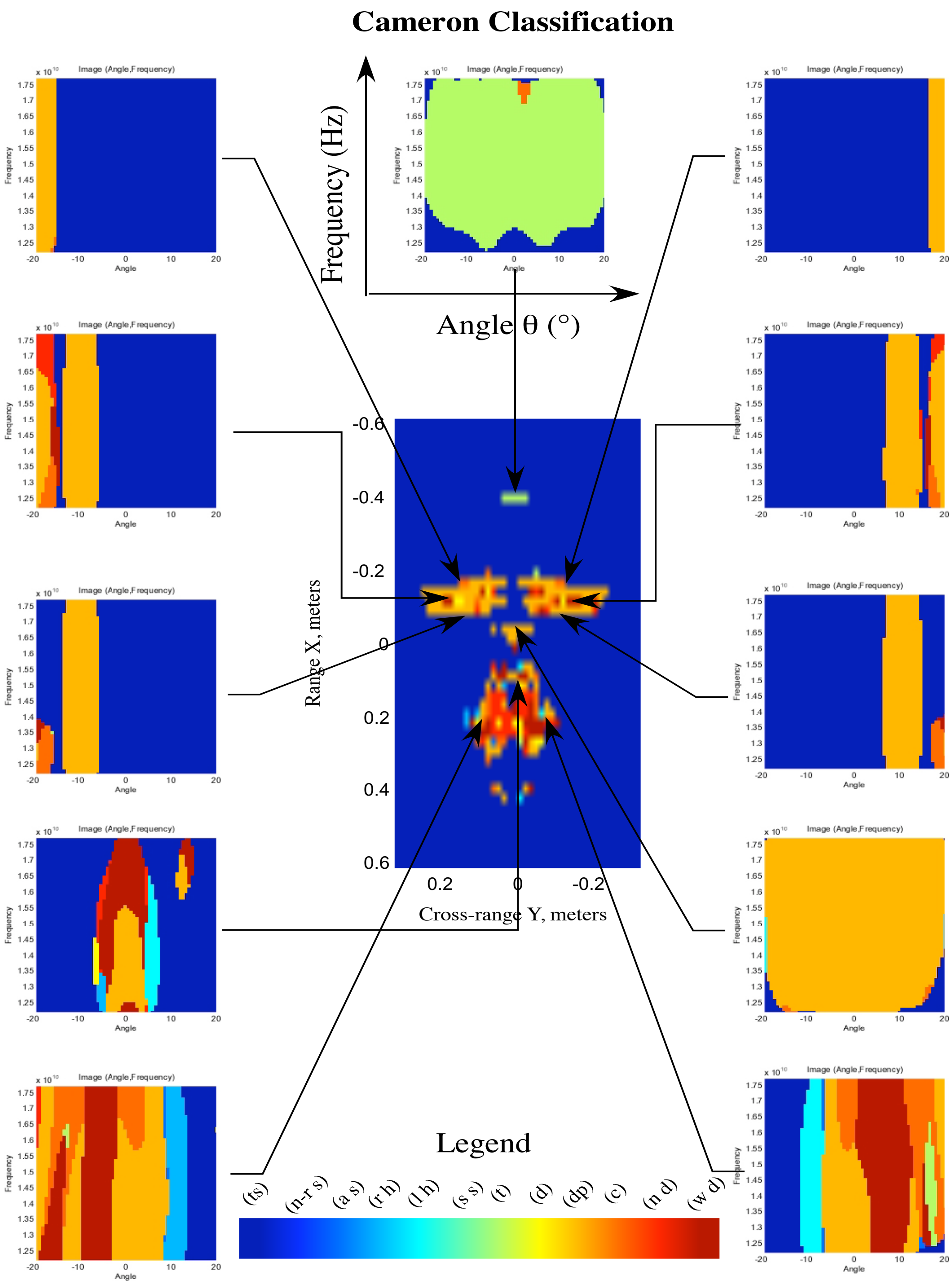

Figure 7 *Cameron classification of hyper-scattering matrices*

$\theta \simeq \pm 10^{\circ}$, the observation of two perpendicular edges (two dipoles) in the same resolution cell induces a helix contribution. For $\theta \simeq \pm 20^{\circ}$ the stabiliser is masked by the body of the Cyrano weapon and the backscattered energy reaches a minimum.

This analysis shows that the joint use 2D TF analysis and polarimetric decompositions, may provide efficient and highly descriptive features of scatterers, related to their geometry and orientation. Such an approach may be an efficient tool to improve targets recognition based on physical parameters.

6 Classification based on the polarimetric anisotropic and dispersive behaviour of scatterers

Numerous approaches to classify targets using frequency or angular scattering characteristics may be found in the

doi: 10.1049/iet-rsn.2008.0086

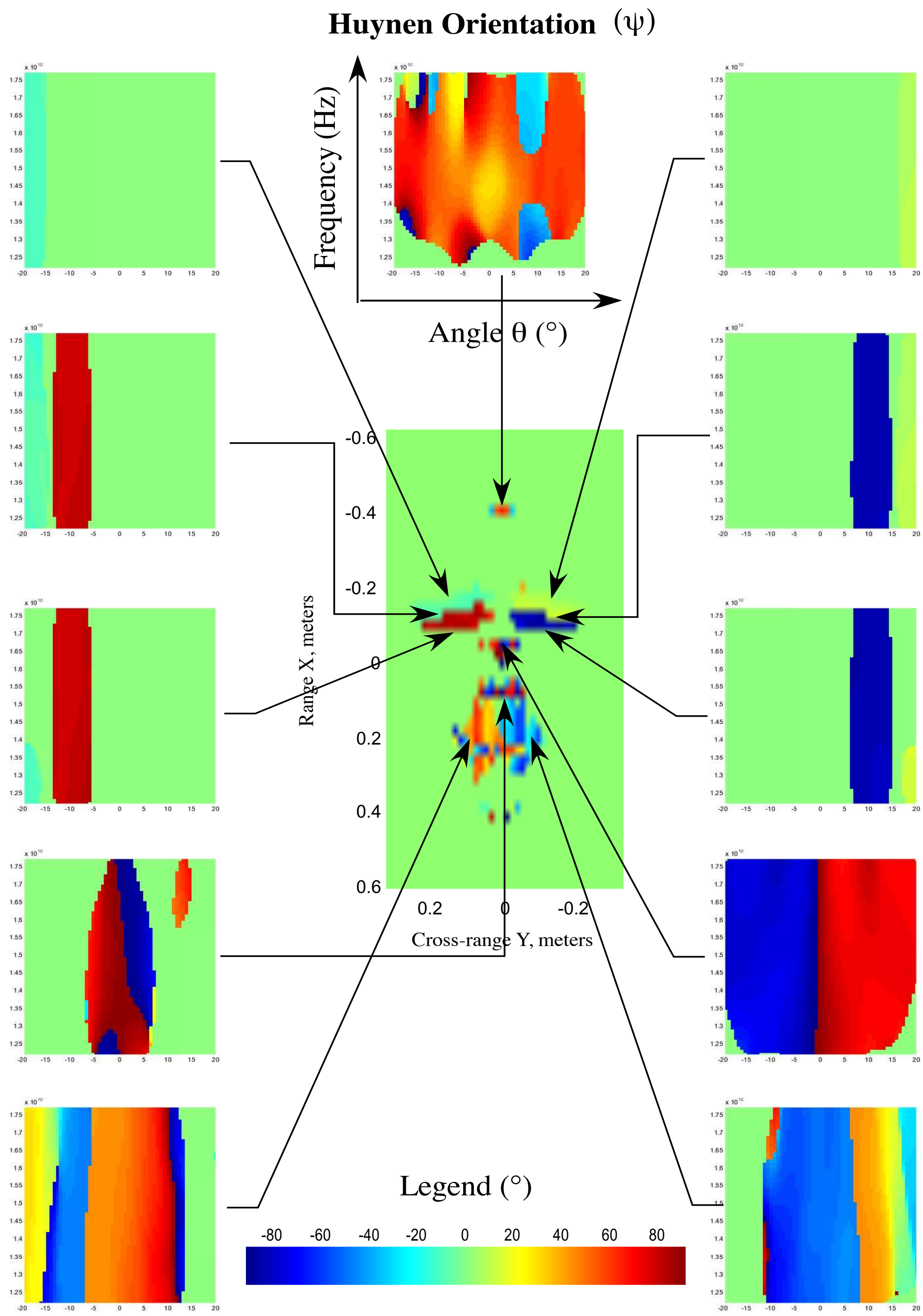

Figure 8 *Huynen orientation derived from the Cameron decomposition*

literature. Among them, one may note the method introduced by Aldhubaib and Shuley [23], based on the determination of an optimal bistatic angle, for which the scattered signal has a robust strength level, irrespective of the target aspect. This optimal bistatic angle concept may then be used to improve the scattered signal-to-noise ratio for targets of interest, prior to classification. Another technique, developed by F. Sadjadi [24], proposes to improve target classification performance using optimum polarimetric SAR signatures that minimise the distance between targets belonging to the same class, while maximising a between class metric.

The classification method we proposed aims to characterise the back-scattering behaviour of a target from characteristic features of its polarimetric hyper-image, that is according to the frequency, angular and polarimetric back-scattering properties of its most significant contributors.

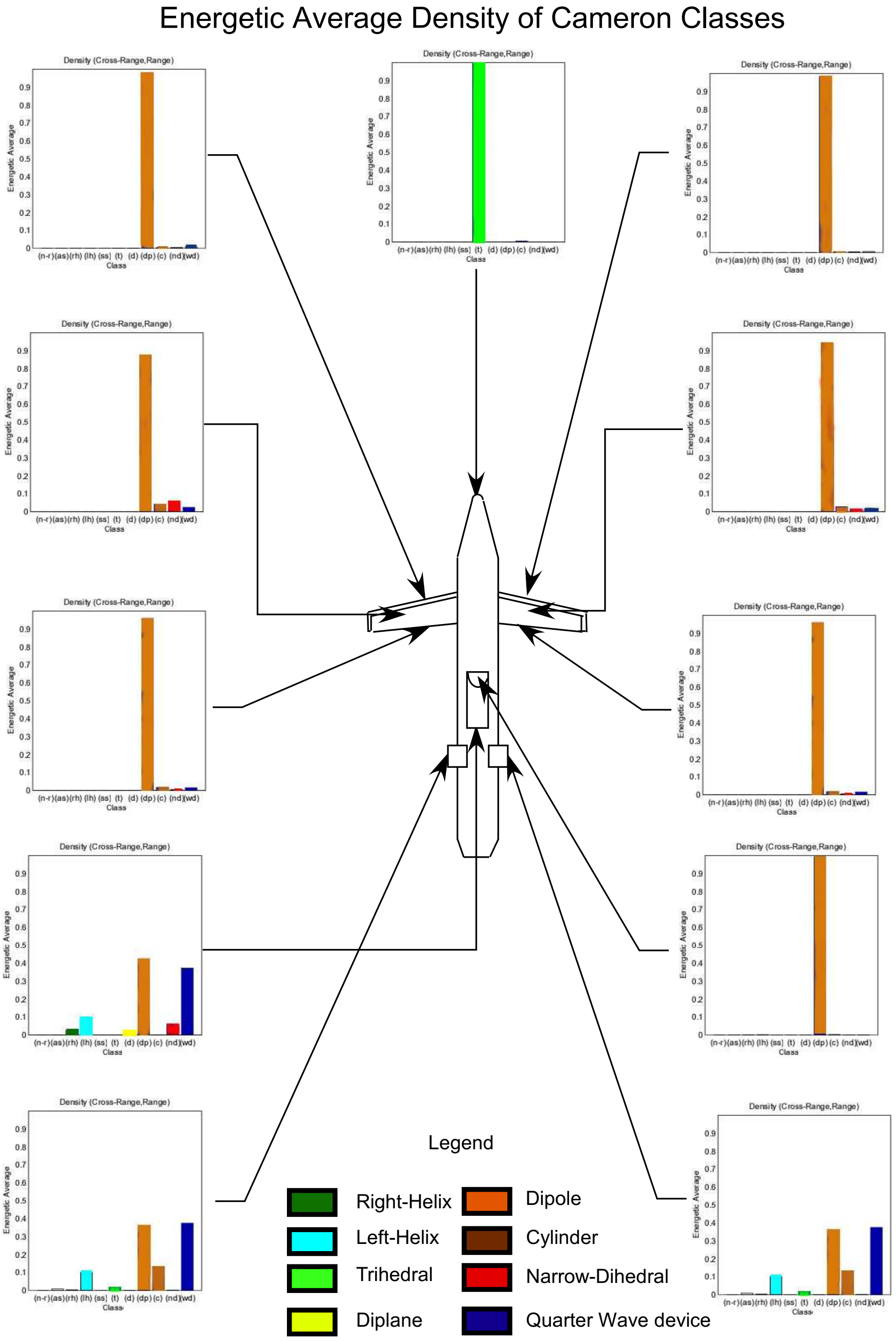

Figure 9 *Average density of polarimetric behaviours*

As revealed by the TF study of the Cyrano weapon model response presented in this paper, some typical properties, like frequency dispersion, angular anisotropy or polarimetric non-stationary polarimetric features, may be efficiently used to discriminate targets. Multidimensional representations, like polarimetric hyper-images, represent a consequent amount of information and may not be well adapted to fast and efficient target classification schemes. In the following, we propose to characterise a target by extracting relevant, orientation independent and highly descriptive indicators from its polarimetric hyper-image and to perform a hierarchical classification of its polarimetric TF behaviour.

6.1 Characteristic TF parameters

As can be seen in Figs. 2, 6 and 7, two kinds of variations of the scattering features in the frequency and angular domains may be considered:

doi: 10.1049/iet-rsn.2008.0086

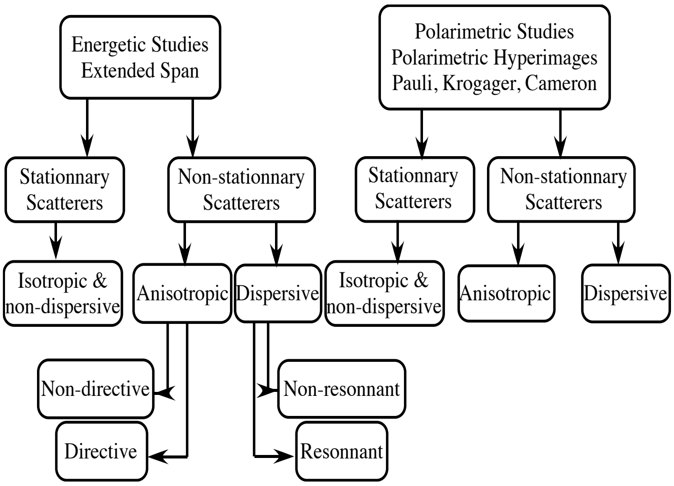

Figure 10 *Propose TF polarimetric classification scheme*

- Energetic variations that modulate the polarimetric signal level and can be characterised using the extended span information.

- Purely polarimetric variations that can be measured in a refined way using output parameters of the Cameron decomposition.

The level of energetic dispersion or anisotropy of a scatterer's response can be quantified by computing the standard deviation of the marginal density of the extended span as

$$\sigma_q(\boldsymbol{r}) = \left[\int_q (q - \mu_q)^2 \, P_q(\boldsymbol{r}, q) \, \mathrm{d}q \right]^{\frac{1}{2}} \quad \text{with} \qquad \mu_q(\boldsymbol{r}) = \int_q q \, P_q(\boldsymbol{r}, q) \, \mathrm{d}q, \;\; q = \theta, f \tag{47}$$

where the marginal densities, $P_f(\boldsymbol{r}, f)$ and $P_\theta(\boldsymbol{r}, \theta)$ are given in (21) and (22), respectively. The resulting indicators of frequency dispersion and angular anisotropy, $\sigma_f(\boldsymbol{r})$ and $\sigma_\theta(\boldsymbol{r})$, respectively, permit to detect efficiently varying energetic behaviours over each part of the measured object.

The amount of polarimetric variability over the frequency–angle domain is estimated from the distribution of the back-scattered energy over the different canonical targets of the Cameron decomposition of the polarimetric hyper image

$$\rho_i(\boldsymbol{r}) = \frac{\int P(\boldsymbol{r}, \boldsymbol{k}) \, \delta(W(\boldsymbol{r}, \boldsymbol{k}) - C_i) \, \mathrm{d}\boldsymbol{k}}{\int P(\boldsymbol{r}, \boldsymbol{k}) \, \mathrm{d}\boldsymbol{k}} \qquad i = 1, \ldots, 10 \tag{48}$$

where $W(\boldsymbol{r}, \boldsymbol{k})$ is hyper-image of the Cameron identification, C_i the ith canonical scattering mechanism and δ the Dirac function.

The characteristic vector, $\boldsymbol{\rho} = [\rho_1, \ldots, \rho_{10}]$, is an histogram that characterises an average energetic polarimetric

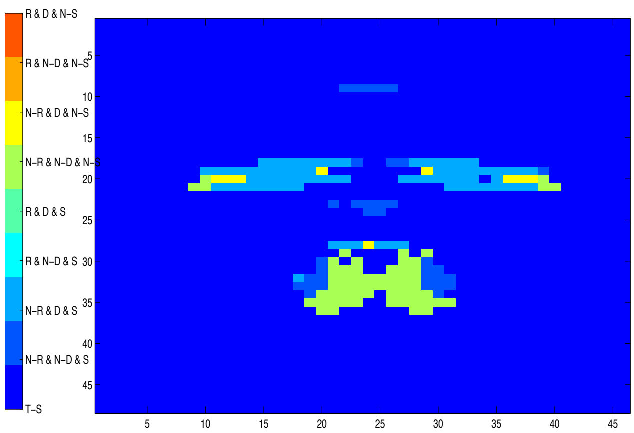

Figure 11 *TF polarimetric classification results*

doi: 10.1049/iet-rsn.2008.0086

Table 2 Legend of TF polarimetric classification results

T-S	thresholded span
N-R	non-resonant
N-D	non-directional
S	polarimetric stationary
R	resonant
D	directional
N-S	polarimetric non-stationary

behaviour in the angular and frequency fields [25] and is illustrated on Fig. 9.

6.2 Classification

The polarimetric TF behaviour of an object may then be characterised using a hierarchical classification scheme, as proposed in [26], presented in Fig. 10. Thresholds for the dispersion and anisotropy indicators are fixed in an automatic way by considering that, due to the intrinsic variability of scattering patterns, the marginal densities of non-dispersive and isotropic scatterers follow a bounded Gaussian distribution $\mathcal{N}(\mu, \sigma)$ whose support is $\pm 3\,\sigma$. For the case under consideration, the angular support being $\Delta\theta = 50^\circ$, $\sigma_\theta(\boldsymbol{r})$ is compared to a threshold equal to 1/6 50°, whereas for a frequency range given by [12, 18] GHz, the threshold for $\sigma_\theta(\boldsymbol{r})$ is fixed at 1 GHz.

A scatterer is considered as having a stationary polarimetric response if one of the Cameron class dominates all the others, that is if there exists $\rho_{\mathrm{i}} \geq 50\%$.

The classification results presented in Fig. 11 with legend given in Table 2 show that the head, the air intake, and the border of stabilisers are classified as non-resonant (N-R), non-directional (N-D), and polarimetrically stationary (S) scatterers. The wings and their edges, the closed air exit are classified as non-resonant, directional, and polarimetrically stationary scatterers. The stabilisers are classified as non-resonant, non-directional, and polarimetrically non-stationary scatterers.

7 Conclusion

In this paper we proposed a new polarimetric TF method that allows to describe the polarimetric behaviour of the scatterers in the frequency and angular domains and is adapted to polarimetric radar imaging. This method is based on the multidimensional wavelet radar imaging method [5] and has been extended to the polarimetric case using coherent polarimetric decomposition methods, like as the Pauli, Krogager and Cameron technique.

This method permits one to discriminate scatterers with a directive, resonant and polarimetrically non-stationary behaviour and allows one to provide physical polarimetric from the extracted scattering mechanisms.

A new classification procedure has been proposed, which allows one to characterise the global polarimetric behaviour of scatterers.

8 References

[1] CHEN V.C., LING H.: 'Time-frequency transforms for radar imaging and signal analysis' (Artech House, Boston, 2002)

[2] SOUMEKH M.: 'Fourier array imaging' (Prentice Hall, Englewood Cliffs, 1994)

[3] SOUMEKH M.: 'Synthetic aperture radar signal processing: with MATLAB algorithms'. (John Wiley, New York, 1999)

[4] BERTRAND J., BERTRAND P.: 'The concept of hyperimage in wide-band radar imaging', 1996, **34**, (5), pp. 1144–1150

[5] OVARLEZ J.P., VIGNAUD L., CASTELLI J.C., TRIA M., BENIDIR M.: 'Analysis of sar images by multidimensional wavelet transform', 2003, **150**, (4), pp. 234–241

[6] TRIA M., OVARLEZ J.P., VIGNAUD L., CASTELLI J.C., BENIDIR M.: 'Discriminating real objects in radar imaging by exploiting the squared modulus of the continuous wavelet transform', 2007, **1**, (1), pp. 27–37

[7] CLOUDE S.R., POTTIER E.: 'A review of target decomposition theorems in radar polarimetry', 1996, **34**, (2), pp. 498–518

[8] MENSA D.: 'High resolution radar imaging' (Artech House, USA, 1981)

[9] FLANDRIN P.: 'Temps-fréquence : deuxième édition revue et corrigée' (Hermes, Paris, 1998)

[10] DUQUENOY M., OVARLEZ J., VIGNAUD L., FERRO-FAMIL L., POTTIER E.: 'Sar imaging using multidimensional frequency'. Proc. Fifth Int. Conf. on Physics in Signal and Image Processing (PSIP'07), 31 January–2 February 2007

[11] JIN T., ZHOU Z., CHANG W.: 'Ultra-wideband synthetic aperture radar time-frequency representation image formation', 2006, **153**, (5), pp. 389–395

[12] FERRO-FAMIL L., REIGBER A., POTTIER E.: 'Nonstationary natural media analysis from polarimetric sar data using a two-dimensional time-frequency decomposition approach', *Can. J. Remote Sens.*, 2005, **31**, (1), pp. 21–29

[13] FERRO-FAMIL L., LEDUCQ P., REIGBER A., POTTIER E.: 'Extraction of information from time-frequency pol-insar response of

doi: 10.1049/iet-rsn.2008.0086

anisotropic scatterers'. Proc. IEEE Int. Geoscience and Remote Sensing Symp. (IGARSS'05), 25–29 July 2005, vol. 7, pp. 4856–4859

[14] POTTER L.C., CHIANG D.M., CARRIÈRE R., GERRY M.J.: 'A gtd-based parametric model for radar scattering', 1995, **43**, (10), pp. 1058–1067

[15] ALBERGA V., KROGAGER E., CHANDRA M., WANIELIK G.: 'Potential of coherent decompositions in sar polarimetry and interferometry'. Proc. IEEE Int. Geoscience and Remote Sensing Symp. (IGARSS'04), 20–24 September 2004, vol. 3, pp. 1792–1795

[16] KROGAGER E.: 'Utilization and interpretation of polarimetric data in high resolution radar target imaging'. Proc. Second Int. Workshop on Radar Polarimetry (JIPR'1992), 8–10 September 1992, vol. 2, pp. 547–557

[17] KROGAGER E., CZYZ Z.H.: 'Properties of the sphere, diplane, helix decomposition'. Proc. Third Int. Workshop on Radar Polarimetry (JIPR'1995), 21–23 March 1995, vol. 1, pp. 106–114

[18] KROGAGER E., DALL J., MADSEN S.N.: 'The sphere, diplane, helix decomposition recent results with polarimetric sar data'. Proc Third Int. Workshop on Radar Polarimetry (JIPR'1995), 21–23 March 1995, vol. 2, pp. 621–625

[19] CAMERON W.L., LEUNG L.K.: 'Identification of elemental polarimetric scatterer responses in high-resolution isar and sar signature measurements'. Proc. Second Int. Workshop on Radar Polarimetry (JIPR'1992), 8–10 September 1992, vol. 1, pp. 196–205

[20] CAMERON W.L., YOUSSEF N.N., LEUNG L.K.: 'Simulated polarimetric signatures of primitive geometrical shapes', 1996, **34**, (3), pp. 793–803

[21] DUQUENOY M., OVARLEZ J., FERRO-FAMIL L., VIGNAUD L., POTTIER E.: 'Study of dispersive and anisotropic scatterers behavior in radar imaging using time-frequency analysis and polarimetric coherent decomposition'. Proc. IEEE Radar Conf., 24–27 April 2006, pp. 180–185

[22] DUQUENOY M., OVARLEZ J., FERRO-FAMIL L., VIGNAUD L., POTTIER E.: 'Study of dispersive and anisotropic scatterers behavior in radar imaging using time-frequency analysis and polarimetric coherent decompositions'. Proc. Sixth European Conf. Synthetic Aperture Radar (EUSAR'06), 16–18 May 2006

[23] ALDHUBAIB F., SHULEY N.: 'Optimal radar bistatic angle by statistical analysis of scattering patterns'. Proc. Asia-Pacifique Conf. on Applied Electromagnetics, 4–6 December 2007

[24] SADJADI F.: 'improve target classification using optimum polarimetric sar signatures', 2002, **38**, (1), pp. 38–49

[25] DUQUENOY M., OVARLEZ J., VIGNAUD L., FERRO-FAMIL L., POTTIER E.: 'Classification based on the polarimetric dispersive and anisotropic behavior of scatterers'. Proc. third Int. Workshop on Science and Applications of SAR Polarimetry and Polarimetric Interferometry (POLINSAR'07), 22–26 January 2007

[26] DUQUENOY M., OVARLEZ J., FERRO-FAMIL L., POTTIER E., VIGNAUD L.: 'Characterization of scatterers by their anisotropic and dispersive behavior'. Proc. IEEE Int. Geoscience and Remote Sensing Symp. (IGARSS'07), 23–27 July 2007

doi: 10.1049/iet-rsn.2008.0086